JOURNAL OF PROPULSION AND POWER
Vol. 26, No. 4, July–August 2010

Rotating Stall Suppression in Axial Compressors with Casing Plasma Actuation

Huu Duc Vo*
École Polytechnique de Montréal, Montréal, Quebec H3T 1J4, Canada

DOI: 10.2514/1.36910

This paper proposes the use of single dielectric barrier discharge, or plasma, actuators to suppress rotating stall inception and extend the stable operating range of axial compressors. Plasma actuators may provide a practical low-power alternative to effectively increase the surge margin of aircraft engines with minimal or even positive impact on compressor performance. A computational study is carried out on a representative subsonic modern compressor rotor geometry to evaluate the proposed casing plasma actuation for suppression of short (spike) as well as long (modal) length-scale rotating stall inception based on their respective flow physics. The objective is to assess the optimum actuator location and required actuation strength to achieve the desired effects at low and medium subsonic compressor speeds. Results show that plasma actuation near the rotor leading edge and concentrated in the tip clearance gap region most effectively suppresses both of the criteria for spike stall inception and delays the predicted stall point to a lower flow coefficient with relatively low power input. In addition, the observed increase in rotor pressure-rise characteristic from the proposed actuation means that the concept, with a new suggested actuator modification, can also be used to suppress modal stall inception. The simulations indicate that actuation effectiveness decreases with increasing rotor tip speed, that the required actuator strength scales with this speed, and that stronger actuation strength than that of conventional single dielectric barrier discharge plasma actuators may be needed. Some implications for the practical implementation of this concept on real compressors are also discussed.

Nomenclature

P	=	static pressure
Pt	=	stagnation pressure
Vx	=	axial velocity
U_{tip}	=	blade (circumferential) tip speed
ρ	=	density
ϕ	=	flow coefficient, $Vx_{\text{in,average}}/U_{\text{tip}}$
ψ	=	total (stagnation)-to-static pressure-rise coefficient, $(P_{\text{out}}\text{-}Pt_{\text{in}})/0.5\rho_{\text{in}}U_{\text{tip}}^2$

I. Introduction

ENGINE surge is a major limiting factor in the operating envelop of aircraft gas turbine engines and is a concern in every new engine design. It can occur at critical operating regimes such as takeoff, maneuvers, and engine acceleration. It is characterized by axisymmetric flow oscillations across the entire engine that leads to a sudden drop in engine power and engine damage whose severity depends on strength of the surge. Surge is a system instability associated with the interaction of the compressor with the combustor and turbine and is usually triggered by rotating stall. Rotating stall is a well-known compressor aerodynamic instability that occurs as the mass flow through the compressor is decreased at a certain speed, as depicted on the compressor map in Fig. 1. It is characterized by the formation of a cell of axial velocity deficiency that rotates as a fraction of the compressor rotor speed and it usually results in a drop compressor pressure rise. Thus, preventing surge usually implies preventing rotating stall. However, as shown in Fig. 1, the common practice of incorporating a safety margin against stall can prevent the compressor from operating at peak efficiency and peak pressure ratio, both of which would thus be located between the resulting operating point and the stall point. The solution would be to suppress rotating stall and move the stall point to a lower mass flow with minimal impact on pressure rise and efficiency, so as to put the design point closer to the optimum location on the compressor map. This can be done more effectively with the understanding of the flow physics of rotating stall inception.

Two routes to rotating stall have been identified in axial compressors: long-length-scale (modal) and short-length-scale (spike) stall inception [1], as illustrated in Fig. 2. Modal stall inception is characterized by the evolution in tens of rotor revolutions of a small full-span disturbance of circumferential wavelength on the order of the annulus into a full rotating stall cell and has been shown to occur at, or slightly beyond, the zero-slope peak of the stagnation-to-static pressure-rise characteristics (speed line) of the compressor (Fig. 2a). It has been understood and successfully modeled [2]. The associated physics can essentially be described as a growth of disturbances in the compression system as the damping goes from positive (negative speed-line slope) to negative (positive speed-line slope). The relatively slow growth rate and initial low amplitude of the modal disturbance means that its individual spatial (circumferential) harmonic can be by suppressed separately with low power actuation that introduces corresponding low-amplitude phase-shifted perturbations. This is the basis of previous successful active control of modal stall inception using movable inlet guide vanes [3], tip jet injection [4,5], and full-span jet injection [6]. The effectiveness of the actuators depends on how well they can produce the circumferential sinusoidal perturbation associated with each controlled harmonic, the amplitude of the perturbation they can produce and their bandwidth, since the induced perturbations must rotate with the corresponding modal disturbance harmonics.

However, many modern compressors stall at a negative slope of the speed line, thus even before reaching the peak pressure rise associated with modal stall inception, instead exhibiting spike stall inception. As illustrated in Fig. 2b, this other type of stall inception starts with the appearance of a sharp local disturbance (spike) at the rotor tip, only two to three blade passages in width, which grows into a fully developed rotating stall cell within roughly three rotor revolutions. The lack of understanding of spike stall inception, the

Presented as Paper 2007-3845 at the 37th AIAA Fluid Dynamics Conference and Exhibit, Miami, FL, 25–28 June 2007; received 29 January 2008; revision received 15 April 2009; accepted for publication 15 April 2009.

*Assistant Professor, Department of Mechanical Engineering, 2900 Boulevard Édouard-Montpetit, 2500 Chemin de Polytechnique, Room C318.9. Member AIAA.

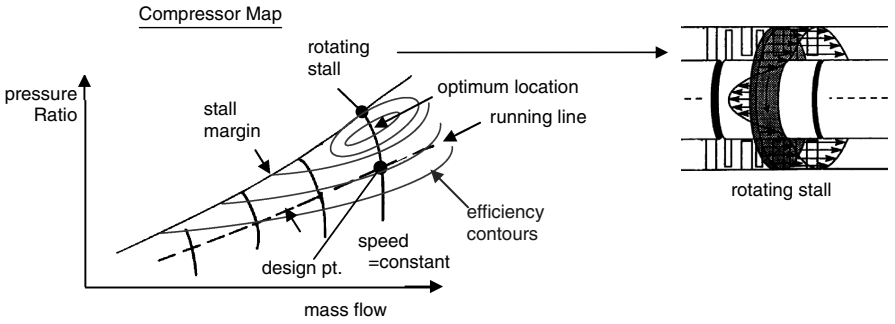

Fig. 1 Rotating stall.

localized nature of the disturbance and short time scales have traditionally made practical detection and active suppression very hard to achieve. A recent numerical study [7] proposed a plausible mechanism to explain short-length-scale rotating stall inception based on tip clearance flow.

As illustrated in Fig. 3, tip clearance flow is the flow through the clearance between the rotor blade tip and compressor casing, driven by the pressure difference across the rotor blade (blade loading). Because of the shear losses within and at the exit of the tip clearance, this fluid that comes out almost normal to the blade camber has high entropy. It then encounters the low-entropy incoming flow to form an interface that is defined by a region of high entropy gradient. The high-loss (low Pt) tip clearance fluid also forms a region of low streamwise velocity that is equivalent to an aerodynamic blockage, which reduces the pressure rise across the blade passage. The position of the incoming/tip-clearance flow interface results from a balance between the momentum of the incoming flow and that of the tip clearance flow. As the flow coefficient decreases, the axial momentum of the incoming flow reduces. At the same time the blade loading and thus the tip clearance flow momentum increases resulting in a movement of the interface toward the rotor leading-edge plane and the blockage in the tip region increases.

Vo et al. [7] postulate that two threshold flow events (and corresponding criteria) associated with the tip clearance flow must be simultaneously present for spike disturbances to form and thus spike stall inception to occur. As illustrated in Fig. 4, these events are as follows:

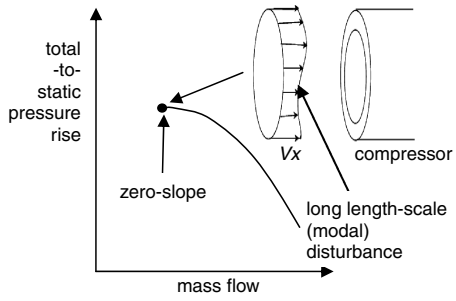

a) Long length-scale (modal) stall inception

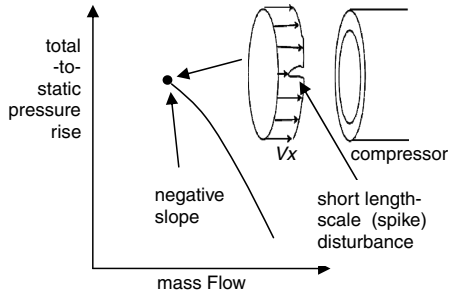

b) Short length-scale (spike) stall inception

Fig. 2 Rotating stall inception routes.

1) Tip clearance flow spillage below the leading-edge (LE) rotor blade tip (Fig. 4a). The onset of this phenomenon is associated with the trajectory of the interface between the incoming and tip clearance flows lining up with the blade tip LE plane.

2) Axial flow reversal (backflow) of tip clearance fluid below the rotor trailing-edge (TE) blade tip impinging on the pressure surface of the adjacent blade (Fig. 4b). This event is indicated by negative pitch-averaged axial velocity or mass flow (i.e., axially upstream flow) below the TE blade tip.

The important point to note is that the above criteria for spike stall inception can be evaluated with single-blade-passage computations. Vo et al. showed that the converged flow solution limit (equilibrium flow limit) in single passage simulations due to the proposed criteria does indeed lead in equivalent multiple-blade-passage simulations to the formation and growth of spike disturbances, as shown in Fig. 5 for a time instant during this process. The flow behavior in Fig. 5 has been experimentally measured on three low-speed single stage axial compressors [8] and a computational study for a transonic rotor [9] also support the proposed spike formation criteria. Two important implications from the work by Vo et al. for the prediction and suppression of spike stall inception are the following:

1) Single-blade-passage computational fluid dynamics (CFD) simulations could be used to predict spike stall inception.

2) Any technique that delays one of the two criteria for spike formation will suppress spike stall inception.

The first statement means that low-cost single-blade-passage CFD simulations could be used to evaluate and optimize the effectiveness of flow control strategies for suppressing spike stall inception before experiments are done. The second statement implies that relatively low-power actuation aimed exclusively at the rotor tip region should be sufficient in suppressing spike stall inception by providing the extra incoming flow momentum needed to at least delay the leading-edge spillage of the tip clearance flow. This is supported by the success of recent experiments in delaying spike stall inception using discrete casing micro injectors upstream of the compressor rotor with diameter in the order of the tip clearance size [8,10]. As opposed to casing treatment (the common present solution to stability problem), these small and low mass flow injectors should not incur any significant compressor/engine efficiency penalty in return for stall margin improvement. However, the risk of clogging in a realistic dirty operating environment and the possible weight and engine integration issues associated with the required piping are potential obstacles to their implementation on real aeroengine designs.

Single dielectric barrier discharge (SDBD) plasma actuators provide an interesting alternative that, if it can be shown to work, could be very attractive to aeroengine manufacturers. As shown in Fig. 6, an SDBD actuator essentially consists of two offset thin electrodes, one of which is exposed to the air, and the other encapsulated in a dielectric material. When an AC voltage of several kilovolts at a frequency of several kilohertz is applied, weakly ionized gases (plasma) are cyclically generated over the encapsulated (hidden) electrode. This plasma generation process does not involve any significant heating of the air and is sustainable at atmospheric pressure. The ionized air is subjected to an electric force in the presence of the electric field created by the electrodes. The result is an induced body force on the rest of the air in this region, which creates a

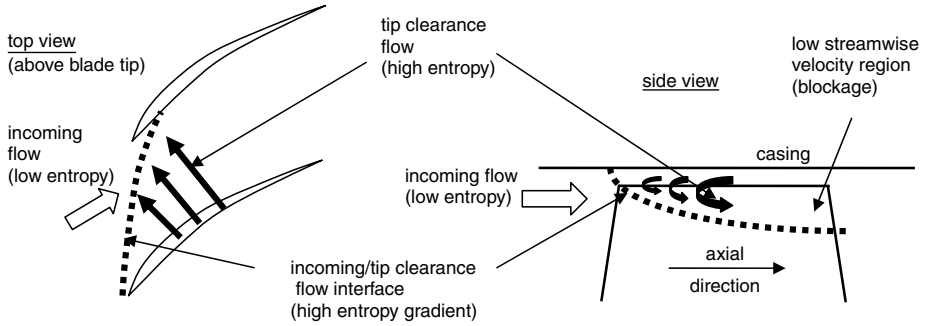

Fig. 3 Incoming/tip-clearance flow interface [7].

very thin jet adjacent to the surface. A more detailed description of the plasma generation and momentum induction process during the voltage input cycle is given in [11,12].

Applications of plasma actuators for flow control have been growing in the past few years [13]. These actuators have been tested in flows with Reynolds numbers up to the 10^5 range to suppress boundary-layer separation on airfoils [14–16] and diffuser walls [17] and to alleviate turbine aerodynamic losses using actuators mounted on the blade tip to effectively reduce the tip clearance gap [18]. Plasma actuators have also been applied at much higher flow velocity to influence boundary-layer instabilities [19] on a sharp cone at Mach 3.5.

Based on the flow physics associated with rotating stall inception, this paper proposes to use plasma actuators on the casing to suppress stall inception. Figure 7 shows the proposed layout, which consists of two stationary thin annular (full-circumference) electrodes mounted on the casing near the rotor. The first application would be to suppress spike stall inception, as depicted in this figure. The body force induced by the plasma actuator should add momentum to the flow in the tip region. Since the trajectory of the interface between the incoming and tip clearance flows is determined by the balance between their momentums (Fig. 3), the proposed actuation should move this interface downstream of the leading-edge plane and thus suppress spillage of tip clearance flow below the leading-edge blade tip (spike criterion 1). Moreover, there may also be a positive effect on tip clearance backflow below the trailing-edge blade tip (spike criterion 2). According to the projected effect on the velocity triangles depicted in Fig. 7b, it is noted that the effect of actuation should be kept within the tip clearance flow region so as not to reduce the tip incidence and thus tip blade loading, which could negatively affect the stage pressure rise. Furthermore, if the proposed casing plasma actuator can induce a noticeable effect on the pressure-rise characteristics, modifications can be proposed for its use to also suppress modal stall inception.

In contrast to discrete high-speed micro jet injection [8,10], the question is whether low-speed circumferentially distributed jet injection with plasma actuators whose region of effective flow acceleration above the surface could be as low as a fraction of a millimeter thick [12] could work. A preliminary computational assessment [20] of the proposed concept had been done with the plasma actuator model proposed by Shyy et al. [12]. Although this

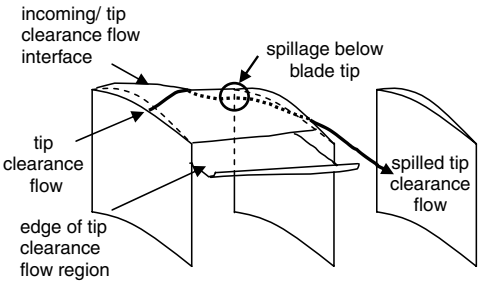

a) Leading-edge tip clearance flow spillage below blade tip (spike stall criterion 1)

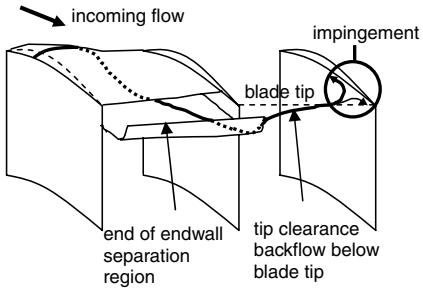

b) Reversal (backflow) of tip clearance fluid below trailing-edge blade tip (spike stall criterion 2)

Fig. 4 Threshold events and corresponding criteria for spike rotating stall inception [7].

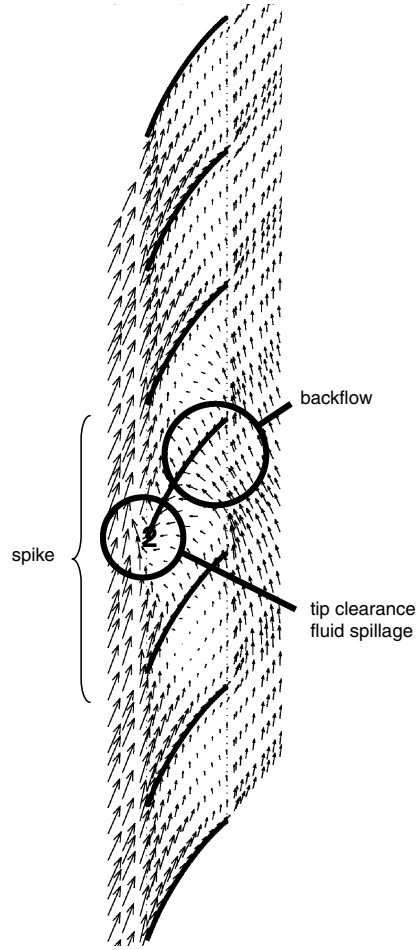

Fig. 5 Spike formation and associated criteria at the blade tip span at a time instant during spike stall inception in multiple-blade-passage CFD simulation [7].

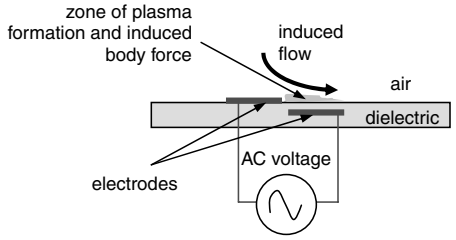

Fig. 6 Plasma actuator.

initial study showed very promising results, the induced body force predicted by the model by Shyy et al. is significantly higher than that measured for conventional SDBD plasma actuators [21,22], and the assessment was only done for a low compressor speed.

The objective of this paper is to assess the following:

1) How effective is the proposed plasma actuation in delaying the spike stall inception criteria at low and medium subsonic compressor speeds in terms of actuator strength and location?

2) Can this concept be used to suppress modal stall inception?

In taking advantage of the implications from the results by Vo et al. [7], we proceed with a computational approach using the flow physics of spike formation and single-blade-passage CFD simulation for a low-speed rotor geometry that is representative of modern subsonic compressor design.

The next section of the paper will present the selection of a model to obtain a representative body-force distribution for plasma actuation and its numerical implementation in an established turbomachinery CFD code. The compressor geometry and numerical procedure will also be described. Subsequently, the results from the numerical simulations will be presented and discussed, followed by the main implications and conclusion.

II. Computational Approach

A. Actuator Model

In the past few years, many models have been developed, with varying complexity, to simulate the fluid dynamic effect of plasma actuators for flow control. The simplest model [23] followed a potential flow approach by modeling the actuator as a doublet for use in a panel method code. Roth [24] modeled the plasma–fluid dynamics coupling in one dimension with an electrostatic body force based on charge density. Shyy et al. [12] produced a more sophisticated model that approximates the effect of a SDBD plasma actuator as a time-averaged linear spatial body-force distribution with a prescribed rough variation with the actuator size and input voltage amplitude and frequency. However, the exact effects of actuator geometry and the nature of the dielectric material on the induced body-force distribution are not captured. Recently, Suzen et al. [25] proposed a model that gives a more accurate body-force distribution by solving for the electric potential field and charge distribution around the actuator, taking into account the exact actuator geometry and the nature of the fluid and dielectric material. However, by solving for a force field at the peak voltage in the cycle and modulating it with actuator input voltage, this model does not capture the experimentally measured variation in time-averaged body force with frequency [21,22]. Orlov et al. [26] are developing a promising model that uses a network of electrical elements to model the glow discharge region over the encapsulated electrode to obtain a more accurate spatial, time and frequency variation of the induced body force. The latest and most sophisticated models [27–29] couple the equations governing the motion of ions and electrons to the flow equations. However, these models are very costly to implement in terms of time and resources and are not considered viable for the present study.

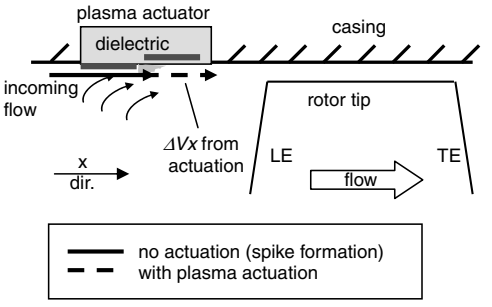

a) Side View

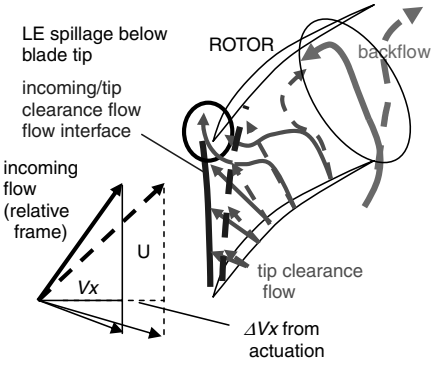

b) Top View: radial plane at blade tip

Fig. 7 Concept of plasma flow actuation for suppression of rotating stall inception [20].

The time-averaged spatial body-force distribution approach provides the most effective modelling of plasma actuation for flow control in complex internal flow problems as it captures the net spatial effect of the actuation on the flow near surface boundaries without adding much computational cost. According to Orlov et al. [26], the time scales associated with the ionization and with the AC input cycle of the actuator are, respectively, six and two orders of magnitude faster than the response of the flow. In other words, the plasma formation process is quasi-instantaneous from the point of view of the flow, thus allowing for the use of a time-averaged body-force distribution. Post and Corke [30] showed that simulations with this approach can reproduce the measured induced velocity profile downstream of a plasma actuator in otherwise quiescent air. This was thus the approach used in our initial study [20] of the proposed casing plasma actuation concept, in which the actuator input voltage and frequency were specified to obtain a time-averaged body-force distribution with the model by Shyy et al. [12]. However, in addition to the approximate (empirical) nature of the spatial body-force distribution in this model, comparison of its predictions with measurements [21,22] show that it over predicts the induced body force by an order of magnitude for the same actuator input voltage and frequency, even though this rough body-force distribution can induce a velocity profile [12] in static air very similar to a measured profile [30]. Nonetheless, to the author's knowledge, no model has yet been validated in terms of giving an accurate body-force distribution with respect to actuator geometry and input. Thus, the proposed revised approach consists of using a more accurate representative spatial body-force distribution and scaling it to assess the effectiveness of plasma actuation with respect to total induced body force (rather than input voltage and frequency), starting from the body-force level measured for conventional SDBD plasma actuators up to that used in the previous study [20].

Among the plasma actuator models of average complexity capable of producing a body-force distribution, the one by Suzen et al. [25] gives the spatial body-force distribution that most resembles those simulated with the most sophisticated models [27–29]. This model was thus used to obtain the representative time-averaged spatial body-force distribution. The associated equations for the electrical potential and charge distributions [25] were discretized in cell-centered form in cylindrical coordinates. They are solved in MATLAB on a fine mesh for an annular plasma actuator on a surface with the casing radius of the compressor geometry to be simulated. Two empirical parameters are needed by the model by Suzen et al. [25]: the Debye length and the maximum charge density. Using the model's suggested Debye length of 0.001 m, the maximum charge

density is obtained by calibrating the model so that it gives a total time-averaged streamwise body force that is similar to the measured value by Baughn et al. [21] for a similar actuator with a similar input voltage. This value comes out to be about 0.004 C/m^3, which is in the range of values obtained from simulations with a more sophisticated model [29]. A representative SDBD plasma actuator is then chosen. As shown in Fig. 8a, it is composed of two 0.1-mm-thick electrodes that are 5 mm wide for the exposed electrode (bottom dark line) and 10 mm wide for the encapsulated (hidden) electrode (top dark line) separated by a Kapton dielectric thickness of 0.34 mm and an axial gap of 0.05 mm. Figure 8a shows the electric potential field solved with the model, which is used with the computed spatial charge distribution (not shown), to give the spatial body-force magnitude distribution and corresponding body-force vectors. These two representations of the spatial body-force distribution are presented in Figs. 8b and 8c for the area delimited by the dashed lines in Fig. 8a. The spatial body-force vector field in Fig. 8c looks qualitatively similar to that obtained with the very sophisticated coupled model shown in [28], with the body-force concentration in the region between the two electrodes having force vectors initially pointing away from the surface and then towards the surface at positions downstream.

According to the chosen model, this actuator should induce a time-averaged total axial body force of about 15 mN/m (millinewtons per meter of actuator length in the circumferential direction) for an input sinusoidal voltage amplitude of 10 kV, which is in the range of conventional SDBD plasma actuators as measured by Baughn et al. [21], but far below the 300 mN/m range given by the model by Shyy et al. [12] for this voltage input [20]. With the chosen thickness of Kapton (dielectric), the voltage amplitude could, in theory. be increased to 50 kV to augment the induced body force by five times. (The actual resulting induced body force may perhaps be even higher than this value if the effect of frequency is taken into account, which cannot be done with this model.) This representative body-force distribution is thus scaled to obtain the total time-averaged induced axial body forces of 15, 76, 153, and 305 mN/m (also referred to in this work as actuator strength) used in this study.

B. CFD Implementation

The CFD code used for this study is UNSTREST [31], a cell-centered 3-D Reynolds-averaged Navier–Stokes time-accurate turbomachinery CFD code with a mixing-length turbulence model and a wall function at solid surfaces. Since the body-force distribution is resolved on a finer mesh than the CFD mesh, the computed spatial body-force distribution is transferred to the CFD mesh by superposing the two grids in the axial–radial plane according to the procedure illustrated in Fig. 9. Each (larger) cell of the CFD grid is placed on top of the body-force grid and the body force associated with the CFD cell is the sum of those from the fine-mesh cells it incorporates, modulated by the percentage of the area of each small cell that lies in the CFD cell. The final body force (per unit depth in the circumferential direction) thus obtained is multiplied by the effective depth of each cylindrical cell (volume/side area) to obtain the total body force for each CFD control volume. The implementation of this procedure in UNSTREST has been verified in our previous study [20], which replicated equivalent simulation results by Shyy et al. [12] for a flat plate.

C. Compressor Rotor

The rotor geometry on which to evaluate the proposed concept is the E^3 rotor B, the first rotor of a GE low-speed constant-radii four-stage research compressor with inlet guide vanes. This compressor has been shown experimentally to stall via spikes originating in the first rotor [32]. This rotor geometry is representative of modern subsonic compressor blading. It has 54 blades with a midspan solidity of 1.16. The hub-to-tip ratio is 0.85 with a constant casing radius of 762 mm. The design speed is 860 rpm, giving a tip Mach number of 0.2 and the Reynolds number based on tip chord is on the order of 300,000. This geometry can also be simulated at 2,150 rpm for a tip Mach number of 0.5. This is the rotor geometry used by Vo et al. [7] to elucidate the mechanism of spike formation.

Figure 10a shows a 3-D view of the $136 \times 41 \times 45$ structured mesh implemented in UNSTREST for time-accurate single-blade-passage simulation of the E^3 rotor B. A pinched blade tip mesh is used. Figure 10b gives a side view of the axial and radial grid near the LE tip clearance gap, with the associated body-force distribution shown in Fig. 8b transferred to the CFD grid using the procedure illustrated in Fig. 9. The nominal tip clearance chosen for study of 1.7 mm (1.8% of tip chord) is shown. To better resolve the effect of actuation, a relatively fine axial and radial CFD grid is used above and downstream of the actuator location. On the other hand, since this is a tip critical rotor, a coarser radial mesh can be used at the hub whose boundary layer need not be resolved in this study. The effect of the small thickness of the exposed electrode on the flow field is neglected and the small protrusion is thus not implemented in the CFD simulation.

Constant inlet stagnation pressure and temperature, as well as a radial distribution of the swirl angle are prescribed at the inlet. The pitch-averaged swirl angle distribution is obtained from the exit flow angle of the inlet guide vanes upstream of this rotor. The exit

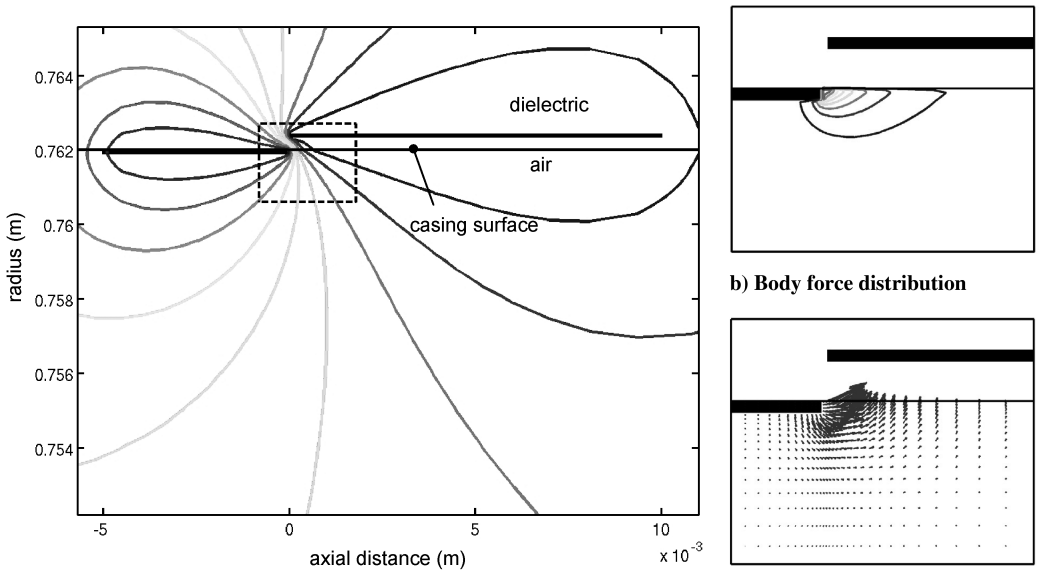

a) Electric potential

b) Body force distribution

c) Body force vectors

Fig. 8 Solving for representative time-averaged spatial body-force distribution.

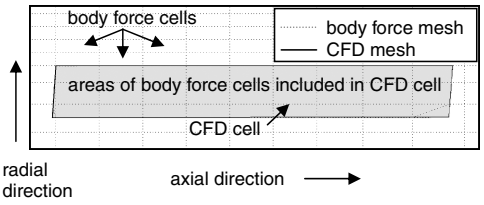

Fig. 9 Determination of body forces for CFD mesh [20].

boundary conditions consist of a constant tip static pressure and radial equilibrium. Accordingly, an inlet duct axial length of one blade pitch is provided to let circumferential potential disturbances on the length scale of the blade pitch decay to zero at the inlet plane. An exit duct of six blade pitches in axial length is provided to insure that any axially reversed flow at the trailing-edge casing due to tip clearance backflow (as depicted in Fig. 4b) gets fully mixed out before reaching the exit plane. The set exit static pressure boundary condition also implies that the simulations cannot capture stable points that lie at a lower mass flow that the point of exit static pressure turnover (zero-slope peak in stagnation-to-static pressure-rise characteristics, associated with modal stall inception). Each time-accurate simulation is considered converged once the mass flow has reached a constant value and remains at this value for several (typically five to 10) blade passing times.

At the first rotor LE on the E^3 compressor, even at the (low) design speed, the Reynolds number on the casing should already be on the order of the transition value for clean flow. Combined with the presence of the upstream inlet guide vanes, a turbulent casing boundary layer can safely be assumed at the actuator location. With the positive pressure gradient in the blade passages, boundary-layer transition is assumed to occur immediately at the blade leading edge. Thus, a turbulent boundary layer is implemented on all surfaces in the simulations.

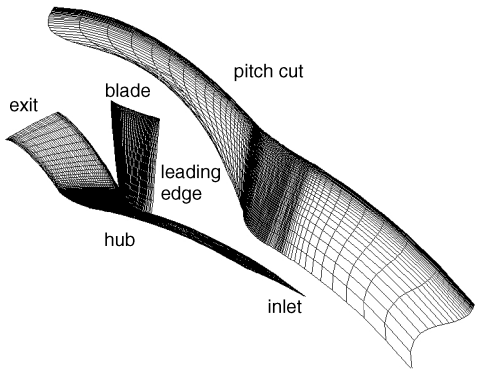

a) 3-D view

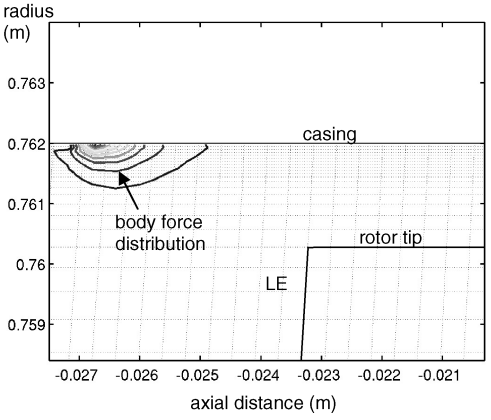

b) Side view of LE tip region

Fig. 10 CFD mesh for E^3 rotor B.

III. Computational Simulations

For each compressor speed under study, the first step of the computational simulation is to find the equilibrium flow (converged solution) limit of the rotor (without actuation) and insure that it is the predicted spike stall inception point through the fulfilment of the two criteria for spike formation depicted in Fig. 4. Starting from a converged solution at high flow coefficient (low pressure rise), the exit tip pressure is increased to obtain a new equilibrium (converged) flow solution (in time-accurate mode). This exit tip pressure is increased incrementally until an equilibrium flow solution no longer exists. This last increment is reduced to get the last converged flow solution close to the equilibrium flow limit.

For the simulation with plasma actuation, our initial study [20] seemed to suggest that the optimum actuator location may be near the rotor leading edge. Thus, as in the initial study, the nominal actuator location for this study is set at 7% of axial chord upstream of the tip leading edge, for which the body-force distribution is shown in Fig. 10b. The actuator location is defined here by the axial position of the axial midgap between the two electrodes. The main intended effect of the actuator location at the leading edge is to move the incoming/tip-clearance flow interface downstream (back into the blade passage) and thus delay the onset of leading-edge tip clearance flow spillage (spike criterion 1). In addition, the effect of trailing-edge actuation will also be verified with the actuator placed inside the blade passage at 7% axial chord upstream of the rotor trailing edge. The projected effect is to delay the onset of backflow below the blade tip at the trailing edge (spike criterion 2).

Simulations with plasma actuation are first carried out at design speed (860 rpm) with a tip Mach number of 0.2. At the exit pressure corresponding to last stable point of the reference (no actuation) case, actuation with induced time-averaged total axial body forces of 15, 76, and 153 mN/m are applied at the actuator location near the leading edge to assess its effects on the two spike stall criteria and pressure-rise characteristics. Subsequently, the most effective actuator strength is applied to the location near the trailing edge for comparison. An optimum actuator location among the two simulated locations is chosen and the exit static pressure is increased to extend the speed line and evaluate how far the predicted stall point can be delayed.

Thereafter, the above simulations are performed for the same compressor at 2.5 times the design speed for a tip Mach number of 0.5. The goal is to assess the change of actuation effectiveness to get a better idea of the actuation requirements for more realistic compressor speeds. In this higher speed case, the tip clearance has to be slightly reduced from 1.8% to 1.5% of chord to get the spike formation criteria to occur before the exit static pressure turnover (zero-slope peak of stagnation-to-static speed line) and thus be captured by the present simulations. Only the optimum actuator location is simulated, with actuator strengths of 76, 153, and 305 mN/m.

The results from the above computational study and their implications for stall control are presented in the next section.

IV. Results and Discussion

The results from the CFD simulations are presented in Figs. 11–13 in a common form. In each figure, the first plot shows the compressor stagnation-to-static pressure-rise characteristic (speed line), from 25% axial chord upstream of the rotor LE plane (upstream of the plasma actuator) to 6% axial chord downstream of the rotor TE plane. The rotor tip circumferential velocity (U_{tip}) is used as the reference speed for the pressure rise and flow coefficients. The symbols and names associated with the points are consistent throughout all the figures. The number in each point name corresponds to a particular exit tip static pressure setting and the remaining suffix is explained in the legend of the figure. The second plot in each figure shows the entropy contour at the blade tip radial plane for selected points to track the incoming/tip-clearance flow interface trajectory. This interface is seen as a region of high entropy gradient (see Fig. 11b) between the low-entropy incoming and high-entropy tip clearance

fluids. The intersection of this interface with the blade tip LE pressure side marks the onset of tip clearance flow spillage below the LE blade tip (spike formation criterion 1). The last plot in each figure gives the spanwise distribution of nondimensional pitch-averaged mass flow (essentially a pitch-averaged flow coefficient involving also density) at the rotor trailing-edge plane. The value of this parameter at the blade tip is marked with the symbol associated with each point. A value of zero at the tip (intersection with the vertical line) marks the onset of backflow below the TE blade tip (spike formation criterion 2). A negative value indicates TE backflow.

A. E^3 Rotor B at Design Speed

Figure 11 presents the simulation results for the E^3 rotor B at design speed without actuation as obtained in our initial study [20]. Points 1 through 5 are steady (converged) stable operating points. A small increase in exit tip static pressure of 1.8% of dynamic head (based on rotor tip speed, U_{tip}) beyond that of point 5 results in the stall transient along which lie points 6s1 and 6s2. Thus, point 5 is the closest point to the equilibrium flow limit. Figure 8b shows that the incoming/tip-clearance flow interface trajectory has reached the rotor LE pressure surface (trajectory parallel to LE plane) at point 5. Figure 11c indicates that the onset of tip clearance backflow, i.e., the fulfillment of the complementary spike formation criterion, occurs at a flow coefficient just below that of point 5. Beyond the equilibrium flow limit, such as for point 6s1, Figs. 11b and 11c shows, respectively, that the incoming/tip-clearance flow interface has spilled ahead of the LE plane and that backflow has occurred below the TE blade tip. Thus, the equilibrium flow limit is the predicted spike stall inception point. This is further reinforced by the negative slope of the stagnation-to-static speed line at point 5 in Fig. 11a.

Figure 12 shows the effect of flow actuation at design speed. Actuation near the leading edge with axial induced body forces of 15, 76, and 153 mN/m applied with the exit pressure setting of point 5

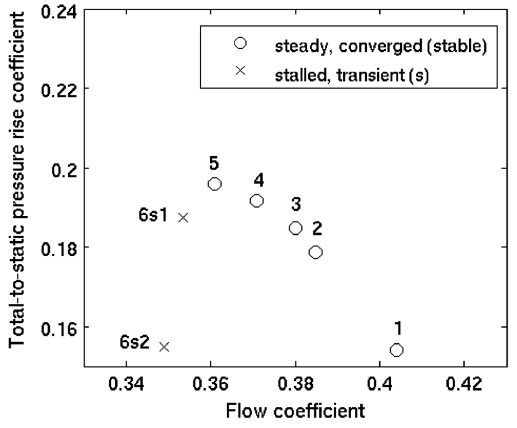

a) Pressure rise characteristic

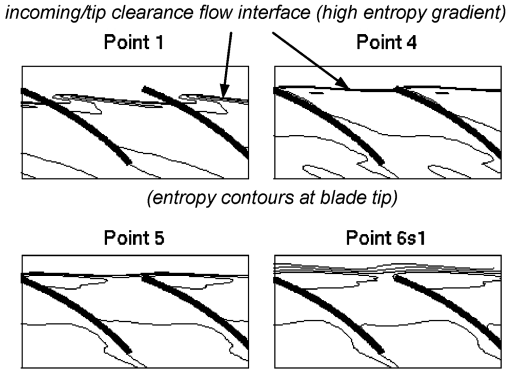

b) Assessment of LE spillage (spike criterion 1)

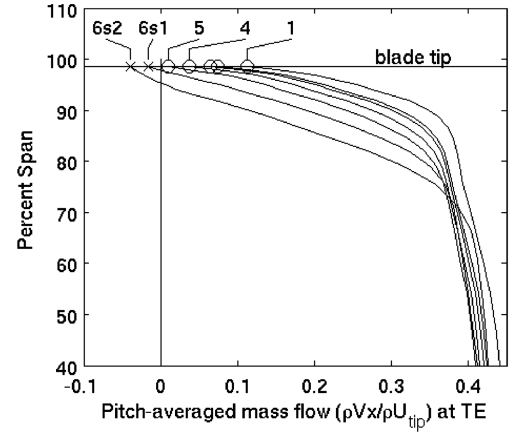

c) Assessment of TE backflow (spike criterion 2)

Fig. 11 Spike stall assessment for E^3 rotor B at design speed without actuation [20].

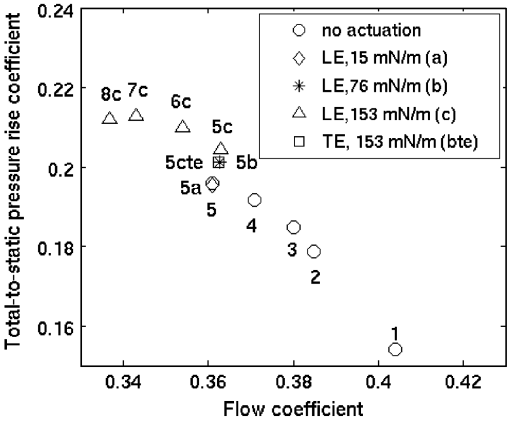

a) Pressure rise characteristic

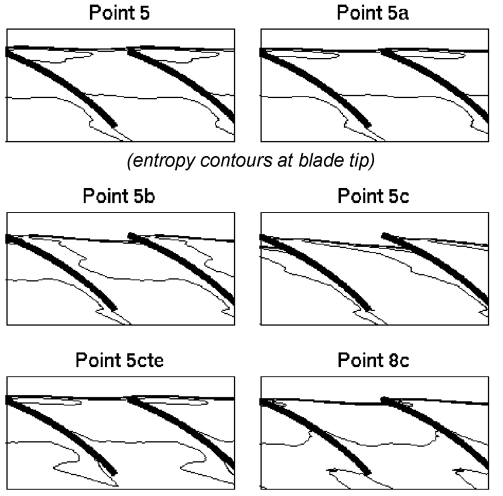

b) Assessment of LE spillage (spike criterion 1)

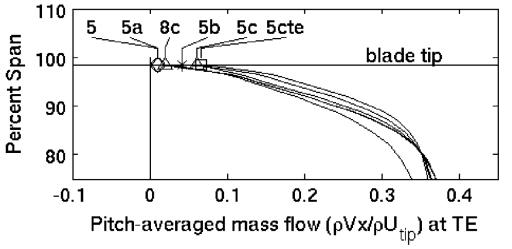

c) Assessment of TE backflow (spike criterion 2)

Fig. 12 Actuation effectiveness at design speed (rotor tip Mach 0.2).

are represented by points 5a, 5b, and 5c, respectively. The results show that an induced body force of 15 mN/m has virtually no effect on the pressure rise or on the two spike formation criteria. This implies that the effectiveness of this level of actuator strength is negligible. However, increasing the actuation strength by five times to 76 mN/m (point 5b) leads to is a positive increase in pressure rise of 2.8% (Fig. 12a) with a noticeable downstream movement of the incoming/tip-clearance flow interface and a significant increase in pitch-averaged mass flow at the trailing-edge blade tip (i.e., delay of TE backflow) according to Figs. 12b and 12c. The increase in pitch-averaged mass flow in the TE tip region also indicates a reduction in tip blockage. Furthermore, the location and extent of the body-force region shown in Fig. 10b points to the induced flow acceleration being radially confined to the tip clearance gap and should thus not reduce the blade tip incidence. (Since this rotor geometry does not exhibit blade boundary-layer separation in the tip region near stall, reducing incidence would have a negative effect on blade tip loading and thus pressure rise.) These two factors should explain the observed increase in pressure rise, which bodes well for performance and for suppressing modal stall inception, as will be discussed later. Doubling the actuation strength to 153 mN/m (point 5c) brings the increase the pressure rise to 4.4%, but has even more significant effect on the incoming/tip-clearance flow interface, while further increasing the pitch-averaged mass flow at the trailing-edge blade tip.

As expected, applying the same actuation strength of 153 mN/m near the trailing edge (point 5cte) does very little to the incoming/tip-clearance flow interface and solely increases tip trailing-edge mass flow. The associated reduction in tip blockage is responsible for an increase in pressure rise of about 2.8%. However, applying the same actuation at the leading edge (point 5c) has about the same effect at the trailing edge while also moving the incoming/tip-clearance flow interface downstream to a position near that corresponding the low-loading point 1, as well as giving a superior pressure-rise increase. This indicates that the actuator location near the leading edge is more optimal.

With 153 mN/m actuation near the leading edge, the exit pressure is increased beyond the nominal stall value associated with points 6s1 and 6s2 to obtain equilibrium flow solution at points 6c, 7c and 8c by delaying the onset of the two spike formation threshold events as shown Figs. 12b and 12c. As the flow is reduced from point 5c to 8c, the incoming/tip-clearance flow interface moves toward the leading-edge and the trailing-edge tip mass flow moves toward zero, as expected, and spike stall inception should eventually occur. However, point 8c, which is at 6.7% below the nominal stall mass flow (point 5) does not represent a spike formation point but is an artificial limit due to fact that the exit static boundary conditions used in this CFD code cannot capture converged solutions much past the point with exit static pressure turnover (around point 7c in this case). (In this case, the static pressure variation along the long downstream duct allowed for the simulations to get converged solutions slightly past the zero-slope peak.)

The above results show that even at the optimum actuator location (in terms of positive effects on spike formation criteria) and for a low compressor tip speed of Mach 0.2, actuator strengths that are several times above those of conventional plasma actuator strength may be needed to have a significant impact on suppressing spike stall inception and a positive impact on pressure rise.

B. E^3 Rotor B at Higher Speed

Figure 13 shows the results for the simulations of the E^3 rotor B at an increased tip speed of Mach 0.5, which should be closer to the operating speeds of most subsonic compressors. Points 11 through 15 are steady (converged) stable operating points. Points 16s1 and 16s2 lie on a stall transient that occurs following an increase in exit tip static pressure of 0.3% of dynamic head (based on U_{tip}) beyond that of point 15. Hence, point 15 is the closest point to the equilibrium flow limit in this case, with both spike formation criteria about to be satisfied at this point according to Figs. 13b and 13c. As in the low-speed case, beyond the equilibrium solution limit, the data for point 16s1 show that the incoming/tip-clearance flow interface has

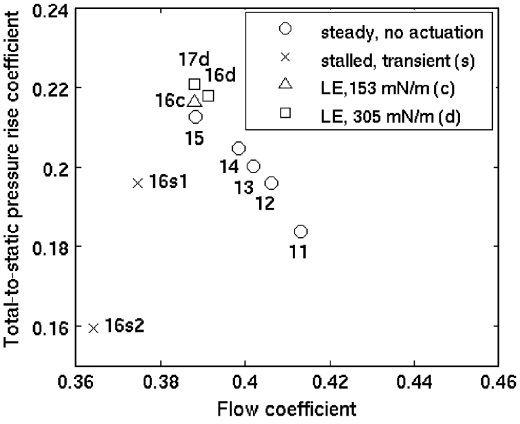

a) Pressure rise characteristic

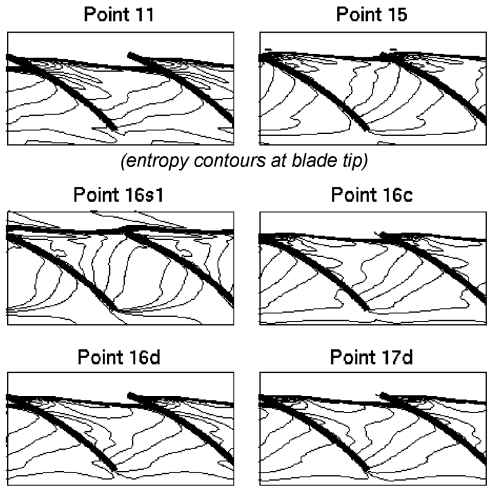

b) Assessment of LE spillage (spike criterion 1)

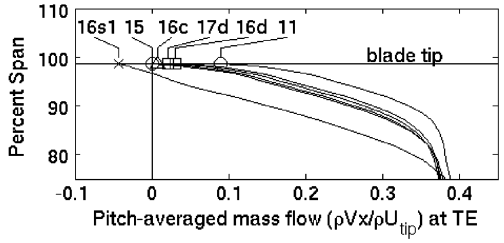

c) Assessment of TE backflow (spike criterion 2)

Fig. 13 Actuation effectiveness at higher speed (rotor tip Mach 0.5).

spilled ahead of the LE plane and that backflow has occurred below the TE blade tip.

Actuation at 7% axial chord upstream of the leading edge is then simulated with actuator strengths of 76, 153, and 305 mN/m, this time at a exit pressure corresponding to the stalled points 16s1 and 16s2. The actuator strength of 76 mN/m (result not shown) could not prevent stall. Compared to the low-speed case (Fig. 12, point 5c), Fig. 13 shows that the 153 mN/m actuation (point 16c) has a significant reduction in effectiveness in terms of pressure-rise increase (only about 1–1.5%) and of the incoming/tip-clearance flow interface and trailing-edge blade tip mass flow. A doubling of the actuation strength to 305 mN/m (point 16d) is required to achieve similar (but still lower) effectiveness than achieved with 153 mN/m at the lower speed case. With this actuation, the exit pressure can increased to further extend the speed line to point 17d and beyond (as shown by the remaining margin in terms of the spike formation criteria assessment in Figs. 13b and 13c at point 17d).

The above results suggest that for increasing rotor speed, the required actuation strength needs to be multiplied by about the same

ratio as the rotor speed. This approximate rule of thumb is demonstrated more precisely in Fig. 14, which shows the effect of LE casing plasma actuation on the incoming/tip-clearance flow interface at different speeds using entropy contours at the blade tip plane similar to those of Figs. 11b, 12b, and 13b. The left plots show the case for point 5 in Fig. 13 (2150 rpm or Mach 0.5 tip speed, 1.5% chord tip clearance) without and with 305 mN/m of actuation. The right plots show the same geometry and tip clearance size, with the rotor tip speed reduced by 2.5 times (860 rpm or Mach 0.2 tip speed) without and with 2.5 times less actuation (122 mN/m). The results point to the same effect on the incoming/tip-clearance flow interface, in terms of the extent of its downstream shift from the leading-edge plane, if the actuation strength is scaled by the blade tip speed.

C. Practical Implications for Stall Suppression

The results from the simulations carried out in the present study have important practical implications in terms of the application of the proposed plasma actuation concept for stall suppression in aircraft gas turbine engines.

First, the results indicate that time-averaged axial induced body forces on the order of 10^2 mN/m will be required to achieve the desired effects of stall margin improvement as well as pressure-rise increase, especially at realistic compressor speeds (a subsequent study by Vo et al. [33] of the same concept for a transonic axial compressor indicates required actuator strength on the order of 1000 mN/m). Although this is an order of magnitude higher than the actuation strength of traditional SDBD plasma actuators based on what has been published in the literature [21,22], these actuator strength levels can be achieved in principle by increasing the applied voltage and frequency beyond the traditional range of 1–10 kV amplitude and 1–10 kHz frequency and by modifications to the actuator geometry, dielectric material, and the shape of the input signal [11], as well as with new input technologies such as nanopulsing [34].

Second, although the results point to the leading-edge region as the best location for a casing plasma actuator, the exact position may depend on the compressor, and CFD simulations may provide an inexpensive tool to find it. Based on the physics, one can deduce that there should be an optimum actuator location with respect to the leading edge. If it is placed too far upstream of the leading edge, the flow acceleration effect at the leading-edge plane is reduced. Moreover, the increase in radial extent of the flow acceleration region will reduce tip incidence and likely the tip blade loading. Although it is conceivable that the resulting reduced momentum of the tip clearance flow would be beneficial in terms of delaying the spike formation criteria and thus delay the stall point, the reduction in pressure rise may not be desirable and may neutralize one major advantage that this type of actuation has over casing treatment, i.e., avoid the tradeoff between performance and stability. On the other hand, while placing the actuator downstream of the leading edge would insure that the actuation does not affect the blade tip incidence, the exposed electrode may be damaged should the rotor tip rub the casing, which could likely happen over the operational life of the engine. Moreover, the influence of the actuation on the incoming leading-edge interface diminishes with increasing actuator distance downstream of the leading edge.

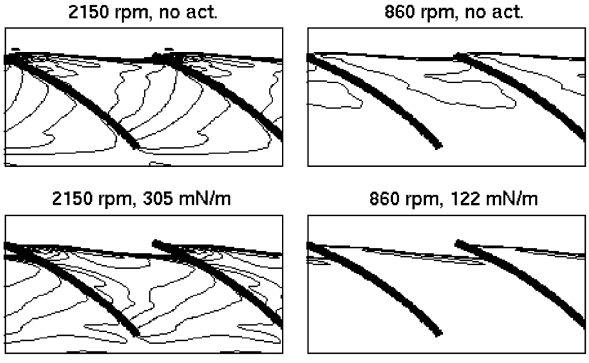

Fig. 14 Effect of plasma actuator strength at different speed for E³ rotor B at 1.5% chord tip clearance.

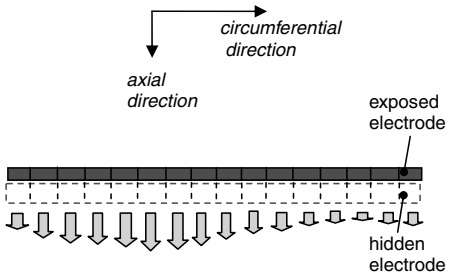

Fig. 15 Proposed actuator modification for modal stall suppression.

Third, although suppressed in one rotor of a multistage compressor, spike disturbances may occur in another rotor at a lower flow coefficient. Thus, there may be a need to apply this concept to multiple rotors in a multistage compressor. In this case, power consumption is one consideration. For the proposed plasma actuation, the power imparted to the flow for the full annulus (computed from the induced body force and the velocity integrated over all cells in the CFD domain) is on the order of 10 W for 153 mN/m actuation strength at the design rotor tip speed of Mach 0.2 and 45 W for 305 mN/m actuation at a rotor tip speed of Mach 0.5. Even if one accounts for the sources of loss associated with plasma actuators [35], the required power levels would still be several orders of magnitude below that needed to drive a compressor. In addition, should power requirements become a concern at higher speeds, one solution would be to apply an optimized on/off (i.e., intermittent) duty cycle to the input so as to excite the turbulent flow structures in the casing boundary layer to obtain momentum transfer from the outer higher-velocity region of the boundary layer rather than from the plasma actuator alone. Another consideration is the geometrical constraint. Because of the limited distance between blade rows, one cannot use multiple actuators in series, which further highlights the importance of fabricating actuators with high induced body forces.

Last but not least, it is noted that modal stall inception will eventually occur once spike stall inception is suppressed and the extended speed line reaches the zero-slope peak, as shown for the 153 mN/m actuation case in Fig. 12a. Thus, a proposed plasma actuation scheme may need to be able to suppress modal stall inception as well. As mentioned earlier, the simulated effects of the proposed plasma actuation on the speed line opens the door for its use to suppress modal stall inception. Indeed, the observed increase in pressure rise on the order of 5% (Fig. 12a) is in line with that of the jet actuators successfully used in experiments to suppress modal stall inception [4–6]. The simulation results also indicate that, if needed, this value can be enhanced with increased actuator strength. As shown in Fig. 15, the proposed actuator can be split into multiple adjacent sections of equal circumferential extent to be able to introduce circumferential perturbations in pressure rise. Since SDBD plasma actuators are relatively simple, the number of adjacent sections can be made high enough to produce purer sinusoidal circumferential perturbations and up to higher spatial harmonics (to control higher modes that usually grow at lower flow coefficients and thus obtain more stall margin) than possible with a limited number of conventional discrete mechanical actuators. At the same time, these actuator sections acting in unison could be used as a single plasma actuator to suppress spike stall inception. Another advantage of plasma actuators for modal stall suppression is that being electrical devices, they should have higher bandwidths than mechanical actuators.

V. Conclusions

A concept for the suppression of spike stall inception with SDBD plasma actuators is proposed. It consists of placing a circumferential plasma actuator on the casing near the compressor rotor to induce axial flow acceleration within the tip clearance gap region to suppress

the tip clearance flow features responsible for spike formation and short-length-scale rotating stall inception. In addition, the proposed plasma actuation could alter the pressure rise enough, through tip blockage reduction, to be used for suppression of modal stall inception. The concept could increase stall margin without affecting the performance of the compressor. A model of an annular SDBD plasma actuator consisting of a time-averaged spatial induced body-force distribution is incorporated into a turbomachinery CFD code. A computational study is carried out to evaluate the concept. The results show that the proposed actuation will work with a sufficiently strong plasma actuator. The required actuator strength scales with the rotor speed. Although the required total induced body force, especially for the higher subsonic speeds, is an order of magnitude higher than that the traditional plasma actuator in the literature, it may not be beyond what can be achieved with improved actuator design and input. The optimum location of the actuator should be very close to the leading edge and should be able to suppress the two criteria for spike stall inception with minimal power consumption. At the same time, limiting the actuation region to within the tip clearance gap should result in an increase of compressor pressure rise, thus not only improving performance, but allow a modification of the actuator to suppress modal stall inception as well.

This concept shows very high potential for significantly improving compressor stall margin and performance with a relatively simple actuator with no moving parts. There are ongoing improvements in plasma actuator design to increase robustness and actuation strength. Early tests have been carried out by Roth et al. [36] to show the robustness of SDBD actuators under wet conditions and their safety when subjected to human handling. Research has also been recently carried out at École Polytechnique de Montréal to demonstrate the operation of SDBD actuators and assess their performance at higher pressures and temperatures toward conditions in the rear stages of compressors. Furthermore, lighter and more powerful power generators for plasma actuators aimed at aerospace applications are becoming commercially available, while the nanopulsing input technology [34] is being developed to provide a step change in actuation strength for the same actuator geometry. These advances should make the experimental validation of the proposed concept for realistic compressor speeds and testing in realistic operating environments possible in the near future.

Acknowledgments

The author would like to thank the Natural Sciences and Engineering Research Council of Canada (NSERC) whose funding was used in part to start this research, O. Toukal at École Polytechnique de Montréal for his assistance in setting up the computational resources, and S. Lemire for his help in the literature search into the very latest and most sophisticated plasma actuation models. Last, but not least, the author would also like to gratefully acknowledge S. Morris and T. Corke of the University of Notre Dame for their insightful comments following the original study of this concept, which helped initiate the revised approach taken to model the plasma actuation.

References

[1] Day, I. J., "Stall Inception in Axial Flow Compressors," *Journal of Turbomachinery*, Vol. 115, No. 1, 1993, pp. 1–9. doi:10.1115/1.2929209

[2] Moore, F. K., and Greitzer, E. M., "A Theory of Post-Stall Transients in Axial Compressors, Part I–Development of Equations," *Journal of Engineering for Gas Turbines and Power*, Vol. 108, No. 1, 1986, pp. 68–76. doi:10.1115/1.3239887

[3] Haynes, J. M., Hendricks. G. J., and Epstein, A. H., "Active Stabilization of Rotating Stall in a Three-Stage Axial Compressor," *Journal of Turbomachinery*, Vol. 116, No. 2, 1994, pp. 226–239. doi:10.1115/1.2928357

[4] Gysling, D. L., and Greitzer, E. M., "Dynamic Control of Rotating Stall in Axial Flow Compressors Using Aeromechanical Feedback," *Journal of Turbomachinery*, Vol. 117, No. 3, 1995, pp. 307–319. doi:10.1115/1.2835665

[5] Weigl, H. J., Paduano, J. D., Frechette, L. G., Epstein, A. H., Greitzer, E. M., Bright, M. M., and Strazisar, A. J., "Active Stabilization of Rotating Stall and Surge in a Transonic Single Stage Axial Compressor," *Journal of Turbomachinery*, Vol. 120, No. 4, 1998, pp. 625–636. doi:10.1115/1.2841772

[6] Vo, H. D., and Paduano, J. D., "Experimental Development of a Jet Injection Model for Rotating Stall Control," American Society of Mechanical Engineers Paper 98-GT-308, 1998.

[7] Vo, H. D., Tan, C. S., and Greitzer, E. M., "Criteria for Spike Initiated Rotating Stall," *Journal of Turbomachinery*, Vol. 130, No. 1, 2008, Paper 011023; also American Society of Mechanical Engineers Paper GT2005-68374, 2005. doi:10.1115/1.2750674

[8] Deppe, A., Saathoff, H., and Stark, U., "Spike-Type Stall Inception in Axial Compressors," *Proceedings of the 6th European Conference on Turbomachinery*, Lille, France, March 2005.

[9] Hah, C., Bergner, J., and Schiffer, H. P., "Short Length-Scale Rotating Stall Inception in a Transonic Axial Compressor: Criteria and Mechanism," American Society of Mechanical Engineers Paper GT2006-90045, 2006.

[10] Nie, C., Xu, G., Cheng, X., and Chen, J., "Micro Air Injection and Its Unsteady Response in a Low-Speed Axial Compressor," *Journal of Turbomachinery*, Vol. 124, No. 4, 2002, pp. 572–579. doi:10.1115/1.1508383

[11] Enloe, C. L., McLaughlin,T. E., Van Dyken, R. D., Kachner, K. D., Jumper, E. J., and Corke, T., "Mechanisms and Responses of a Single Dielectric Barrier Plasma Actuator: Plasma Morphology," *AIAA Journal*, Vol. 42, No. 3, 2004, pp. 589–594. doi:10.2514/1.2305

[12] Shyy, W., Jayaraman, B., Andersson, A., "Modeling of Glow Discharge-Induced Fluid Dynamics," *Journal of Applied Physics*, Vol. 92, No. 11, 2002, pp. 6434–6443. doi:10.1063/1.1515103

[13] Corke, T., and Post, M., "Overview of Plasma Flow Control: Concepts, Optimization, and Applications," AIAA Paper 2005-563, 2005.

[14] Huang, J., Corke, T. C., and Thomas, F., "Plasma Actuators for Separation Control of Low Pressure Turbine Blades," AIAA Paper 2003-1027, 2003.

[15] Post, M., and Corke, T. C., "Separation Control On High Angle of Attack Airfoil Using Plasma Actuators," *AIAA Journal*, Vol. 42, No. 11, 2004, pp. 2177–2184. doi:10.2514/1.2929

[16] Goeksel, B., Rechenberg, I., Greenblatt, D., and Paschereit, C. O., "Steady and Unsteady Plasma Wall Jets for Separation and Circulation Control," AIAA Paper 2006-3686, 2006.

[17] Boxx, I. G., Newcamp, J. M., Franke, M. E., Woods, N. M., and Rivir, R. B., "A PIV Study of a Plasma Discharge Flow-Control Actuator on a Flat Plate in an Aggressive Pressure Induced Separation," American Society of Mechanical Engineers Paper GT2006-91044, 2006.

[18] Morris, S., Corke, T., VanNess, D., Stephens, J., and Douville, T., "Tip Clearance Control Using Plasma Actuator," AIAA Paper 2005-782, 2005.

[19] Corke, T., Cavalieri, D., and Matlis, E., "Boundary Layer Instability on a Sharp Cone at Mach 3.5 with Controlled Input," *AIAA Journal*, Vol. 40, No. 5, 2002, pp. 1015–1018. doi:10.2514/2.1744

[20] Vo, H. D., "Suppression of Short Length-Scale Rotating Stall Inception with Glow Discharge," American Society of Mechanical Engineers Paper GT2007-27673, 2007.

[21] Baughn, J. W., Porter, C. O., Peterson, B. L., McLaughlin, T. E., Enloe, C. L., Font, G. I., and Baird, C., "Momentum Transfer for an Aerodynamic Plasma Actuator with an Imposed Boundary Layer," AIAA Paper 2006-168, 2006.

[22] Porter, C. O., Baughn, J. W., McLaughlin, T. E., Enloe, C. L., and Font, G. I., "Temporal Force Measurements on an Aerodynamic Plasma Actuator," AIAA Paper 2006-104, 2006.

[23] Hall, K. D., Jumper, E. J., Corke, T. C., and McLaughlin, T. E., "Potential Flow Model of a Plasma Actuator as a Lift Enhancement Device," AIAA Paper 2005-783, 2005.

[24] Roth, J. R., "Aerodynamic flow Acceleration Using Paraelectric and Peristaltic Electrohydrodynamic effects of a One atmosphere Uniform Glow discharge Plasma," *Physics of Plasmas*, Vol. 10, No. 5, 2003, pp. 2117–2126. doi:10.1063/1.1564823

[25] Suzen, Y. B., Huang, P. G., Jacob, J. D., and Ashpis, D. E., "Numerical Simulations of Plasma Based Flow Control Applications," AIAA Paper 2005-4633, 2005.

[26] Orlov, D. M., Apker, T., He, C., Othman, H., and Corke, T., "Modeling and Experiment of Leading Edge Separation Control Using SDBD

Plasma Actuators," AIAA Paper 2007-0877, 2007.
[27] Roy, S., Singh, K. P., Kumar, H., Gaitonde, D. V., and Visbal, M. R., "Effective Discharge Dynamics for Plasma Actuators," AIAA Paper 2006-374, 2006.
[28] Gaitonde, D. V., Visbal, M. R., and Roy, S., "A Coupled Approach for Plasma-Based Flow Control Simulations of Wing Sections," AIAA Paper 2006-1205, 2006.
[29] Jayaraman, B., Thakur, S., and Shyy, W., "Modeling of Dielectric Barrier Discharge and Resulting Fluid Dynamics," AIAA Paper 2006-686, 2006.
[30] Post, M. L., and Corke, T. C., "Separation Control on high Angle of Attack Airfoil Using Plasma," *AIAA Journal*, Vol. 42, No. 11, 2004, pp. 2177–2184.
doi:10.2514/1.2929
[31] Denton, J. D., "The Use of a Distributed Body Force to Simulate Viscous Effects in 3D Flow Calculations," American Society of Mechanical Engineers Paper 86-GT-144, 1986.
[32] Silkowski, P. D., "Measurements of Rotor Stalling in a Matched and Mismatched Multistage Compressor," Massachusetts Inst. of Technology, Gas Turbine Lab., Rept. 221, Cambridge, MA, 1995.
[33] Vo, H. D., Cameron, J. D., and Scott, S. C., "Control of Short Length-Scale Rotating Stall Inception on a High Speed Axial Compressor with Plasma Actuation" American Society of Mechanical Engineers Paper GT2008-50967, 2008.
[34] Opaits, D. F., Neretti, G., Likhanskii, A. V., Zaidi, S., Shneider, M. N., Miles, R. B., and Macheret, S. O., "Experimental Investigation of DBD Plasma Actuators Driven by Repetitive High Voltage Nanosecond Pulses with DC or Low-Frequency Sinusoidal Bias," AIAA Paper 2007-4532, 2007.
[35] Roth, J. R., and Dai, X., "Optimization of the Aerodynamic Plasma Actuator as an Electrohydrodynamic (EHD) Electrical Device," AIAA Paper 2006-1203, 2006.
[36] Roth, J. R., Madhan, R. C. M., Manish Yadav, and Rahel, J., "Flow Field Measurements of Paraelectric, Peristaltic, and Combined Plasma Actuators Based on the One Atmosphere Uniform Glow Discharge Plasma (OAUGDP)," AIAA Paper 2004-845, 2004.

A. Prasad
Associate Editor